Single virus detection on silicon photonic crystal random cavities

Keisuke Watanabe, Hsin-Yu Wu, Jolly Xavier, Lovleen Tina Joshi, Frank Vollmer**

Dr. Keisuke Watanabe, Dr. Hsin-Yu Wu, Dr. Jolly Xavier, Prof. Frank Vollmer
Department of Physics and Astronomy, Living Systems Institute, University of Exeter, EX4 4QD, Exeter, UK
E-mail: K.Watanabe@exeter.ac.uk; F.Vollmer@exeter.ac.uk
Dr. Lovleen Tina Joshi
School of Biomedical Sciences, University of Plymouth, Plymouth PL4 8AA, UK

On-chip silicon microcavity sensors are advantageous for the detection of virus and biomolecules due to their compactness and the enhanced light-matter interaction with the analyte. While their theoretical sensitivity is at the single-molecule level, the fabrication of high quality (Q) factor silicon cavities and their integration with optical couplers remain as major hurdles in applications such as single virus detection. Here we propose, and demonstrate, label-free single virus detection using silicon photonic crystal random cavities. The sensor chips consist of free-standing silicon photonic crystal waveguides and do not require pre-fabricated defect cavities or optical couplers. Residual fabrication disorder results in Anderson-localized cavity modes which are excited by a free space beam. The $Q \sim 10^5$ is sufficient for observing discrete step-changes in resonance wavelength for the binding of single adenoviruses (~50 nm radius). Our findings point to future applications of CMOS-compatible silicon sensor chips supporting Anderson localized modes that have detection capabilities at the level of single nanoparticles and molecules.

1. Introduction

The worldwide viral pneumonia outbreak designated as coronavirus disease 2019 (COVID-19) has highlighted the importance of diagnostic and sensing methods for virions and viral molecules.[1] Sensors that can detect a virus rapidly can help track community spread and are emerging as vital tools in gaining control of global health emergencies such as the COVID-19 outbreak. Recent studies have shown the importance of optical sensors for the diagnosis of severe acute respiratory syndrome-coronavirus-2 (SARS-CoV-2), the cause of COVID-19.[1,2]

In response to the need for virus sensing methods, photonic and plasmonic sensors have been developed and used for the detection of coronavirus particles,[3] their viral genomes,[4] and serological antibodies.[5,6]

Some of the most sensitive nanoparticle and molecule detections have been demonstrated with optical microcavities.[7] On-chip detection of biomolecules with optical microcavities is possible on photonic crystal (PhC) sensors.[8–11] Silicon-based PhC sensors can be fabricated as planar devices i.e. on silicon-on-insulator wafers. The quasi two dimensional PhC sensors are a class of optical microcavities that confine the light in particularly small mode volumes in the order of $(\lambda/n)^3$. The small modal volume combined with a reasonably high quality (Q) factor of the silicon microcavities[12] provides a sensitive response of the microcavity to the strong light-matter interaction with an analyte particle.[13] Using chip-scale silicon PhC sensors, the detection of virus-sized particles by the wavelength shift,[11,12,14–16] antibody detection based on near-field optical trapping of virus particles[17] and the detection of viruses by imaging-based techniques[18] have been demonstrated. Silicon PhC sensors provide the platform technology that would be ideally suited for developing much needed virus detection methods, and for meeting the demand for an on-chip sensing platform that is capable of the real-time sensing of single virus particles.[2]

Real-time single virus sensing from the optical shift of a silicon-based microcavity has not been previously reported. Although the PhC cavities have a figure of merit Q/V, where Q is the quality factor and V is the mode volume, that is larger than the Q/V of the whispering-gallery-mode glass microspheres previously used for the detection of small virions[19,20] and single proteins,[21–23] there are challenges in fabricating the high Q/V cavity in silicon and assembling a functioning silicon sensor chip for virus detection in an aqueous solution. Major hurdles have been the integration of an optical coupler for the excitation of the PhC cavity modes, the fabrication of microcavities of sufficiently high Q factors, and coupling the light in and out of the chip for real-time nanoparticle sensing.[24] Couplers such as optical fibres made use of edge-coupling using a spot size converter[25] or tapered fibre coupling[26] in order to excite the microcavity/PhC structures. However, the addition of these fibre-based optical components complicated the measurement system and often limited the sensor's detection capability. Moreover, a fragile taper often makes it difficult to carry out the measurements in aqueous solution without breaking the fibre.[27] Furthermore, the binding of just a few particles to the taper can rapidly degrade the fibre transmission.[28] Detection of several nanoparticles without saturating a PhC microcavity response remains as another challenge.

To overcome these challenges and to achieve the real-time sensing of single virus particles with on-chip silicon microcavity sensors, we utilize silicon PhC *random* cavities in a conventional W1 waveguide.[29,30] The PhC random cavities are excited by a free space beam (**Figure 1**a). Nanoparticle sensing with Anderson-localized, random PhC cavities[30] provides several advantages as compared to the use of other, more carefully engineered PhC defect cavities[31] or PhC heterostructure cavities[32,33]: (1) The silicon PhC sensor consists only of the W1 waveguide without requiring any other pre-fabricated optical structures such as defect cavities or coupler(s); (2) the residual and unavoidable fabrication disorder which usually limits a sensor's performance here localizes the light in the high Q/V random cavities; (3) the excitation of the random cavities along the guide using the free-space beam[34] requires only minimal initial beam alignment; (4) many particles can be detected without saturating a microcavity response, and (5) the free-space excitation allows for ease of integration with an aqueous sample cell and, in the future, with simple microfluidics.

The random cavity modes along the W1 waveguide result from the Anderson-localization of light[30,35–38] because of the coherent multi-scattering at the nanoscale fabrication imperfections of the PhC holes.[39,40] The length-scale of the fabrication disorder is in the order of a few nm in this work, as revealed by scanning electron microscopy (the root-mean-square deviation of air-hole roughness in this work was < 6 nm).[30] Due to the high Q factors in the order of 10^5 (ref. [41]) and the small V in the order of $1(\lambda/n)^3$ (ref. [42]), the Anderson-localized random cavities have previously been used for example in InGaAsP random lasers[43] and for quantum electrodynamics in GaAs PhC waveguides[35] to demonstrate the strong coupling with a single emitter.[44,45] Previously, we have demonstrated $Q > 10^5$ in silicon PhC W1 waveguide slabs in the telecom wavelength range at a similar level of nanoscale disorder,[34,41] and predicted that the Anderson-localized random PhC microcavity sensor could provide a platform suitable for various biosensing applications. Despite this potential for biosensing and nanoparticle detection in particular, there have been very few reports that use the Anderson-localized W1 random cavity modes for sensing applications. Previous works demonstrated temperature sensing based on the thermo-optic effect of silicon[46] and the sensing of the bulk refractive index of the surrounding solution using PhC random cavities fabricated in Si_3N_4.[47]

In this paper, we unveil the sensing characteristics of Anderson-localized modes in silicon PhC waveguide slabs which, at the Q of 10^5, are already sensitive enough to resolve virus-sized (radius ~50 nm) single particle binding events. First, we statistically evaluate the sensitivity of the PhC random cavities to a bulk refractive index change. We characterise the perturbation by the environmental refractive index and demonstrate a large figure of merit of $\sim10^4$ RIU^{-1}. Next,

we experimentally investigate the label-free detection capability with polystyrene nanoparticles that corresponds to the local perturbation of the refractive index and find the minimum detectable nanoparticle radius to be ~34 nm. We demonstrate the single virus particle detection with adenovirus, which has a radius of about 50 nm, with a signal to noise ratio of approximately 4. We find that an Anderson-localized random microcavity is capable of detecting many particle binding events despite its small modal volume on the order of $1(\lambda/n)^3$. We demonstrate the detection of up to 60 nanoparticle binding events from recording the step-wise changes in the resonance wavelength of a single microcavity as the particles bind to the PhC sensor over the course of 20 min. This unexpected result shows that Anderson-localized cavities combine a very high detection sensitivity with a large detection bandwidth, a combination of highly desirable sensing characteristics that will enable developing important on-chip biosensing applications.

2. Results

2.1. PhC random cavities

The PhC structure design used in our experiments is a standard W1 PhC waveguide obtained by leaving out air-holes along the Γ-K direction of the reciprocal-lattice.[48] Figure 1a shows the schematic of the device with the location of the random cavities highlighted. The PhC waveguide has a lattice constant of $a = 410$ nm and the normalized air-hole radius with R/a ~0.3. For the excitation of localized modes, a tightly focused wavelength-tuneable laser beam was focused from vertical direction onto the slab at the end-facet of a waveguide. As we have shown in the previous work, a polarization-tailored beam can excite Anderson-localized modes[34] and the sensor response can be detected with sensitive InGaAs detectors despite the fact that the coupling efficiency is not as large when compared with the commonly-used side/butt coupling or the tapered-fibre coupling[49] methods. The spectrum of the high Q localized modes can be efficiently collected by tuning the laser wavelength and simultaneously recording the light scattered in the out-of-plane direction and focused on a photodetector (Figure 1c). An infrared (IR) camera is used to image the location of the microcavities along the approx. 120 μm long waveguide (Figure 1d). The polarization direction of the linearly-polarized laser light was adjusted to the direction parallel to the waveguide to achieve a better coupling to the waveguide.[34] The residual fabrication disorder inherent in the silicon PhC induces both backscattering and out-of-plane scattering for the light propagating along the W1 waveguide, especially in the vicinity of the cut-off frequency where the radiation losses of the slowly guided Bloch-TE waveguide mode[46] increase.[50,51] As a result, one can vertically

collect the scattered light using an objective to measure the spectrum of the localized modes for those k-vector components that lie within the numerical aperture (NA) of the objective. Since the localized cavities arise from the TE-like fundamental mode, the polarization direction of vertically scattered light is predominantly perpendicular to the waveguide. Thus, the localized modes can be collected by the photodetector using a polarizing beam splitter (PBS) while the background noise coming from the excitation laser is cut out by this cross-polarized configuration.[52,53] In contrast to other resonance scattering methods[54] in which the scattered light experiences Fano interference, our methods give rise to purely Lorentzian lineshapes because the excitation light and the scattered light do not propagate on the same optical path.

Figure 1d shows the spatial maps for the localized modes that were imaged by the IR camera as we step-wise change (sweep) the wavelength of the laser. The linescans were extracted from the images taken of the PhC while in air and after immersing the PhC slab in deuterium oxide (D_2O). The localized states appear in the images as the laser wavelength approaches the band edge of the TE-like W1 waveguide mode. The Anderson-localization of light is seen only in a narrow spectral window which is about 5 nm wide, in this example from about approx. 1550 nm to 1555 nm for a slab immersed in D_2O. We used D_2O instead of pure water (H_2O) to minimise the absorption loss that limits the Q factor of the cavity mode to $\sim 10^4$ in the telecom wavelength range[55] (see Figure S2 and Table S1 for more details and for measurements in H_2O). Due to the increase in the refractive index in aqueous solution as compared to air, the localized modes are red-shifted in D_2O by about 15 nm. After immersing the sensor in the aqueous solution, we observed annihilation and generation of localized modes possibly because the altered refractive index changes the multiple scattering conditions in the waveguide. Figure 1e shows examples of the spectra obtained in air and in D_2O for the same PhC slab. Compared with the measurement in air ($Q = 1.6 \times 10^5$), the Q factor slightly degrades in D_2O ($Q = 1.0 \times 10^5$). We found that this Q is still high enough to carry out the nanoparticle sensing experiments.
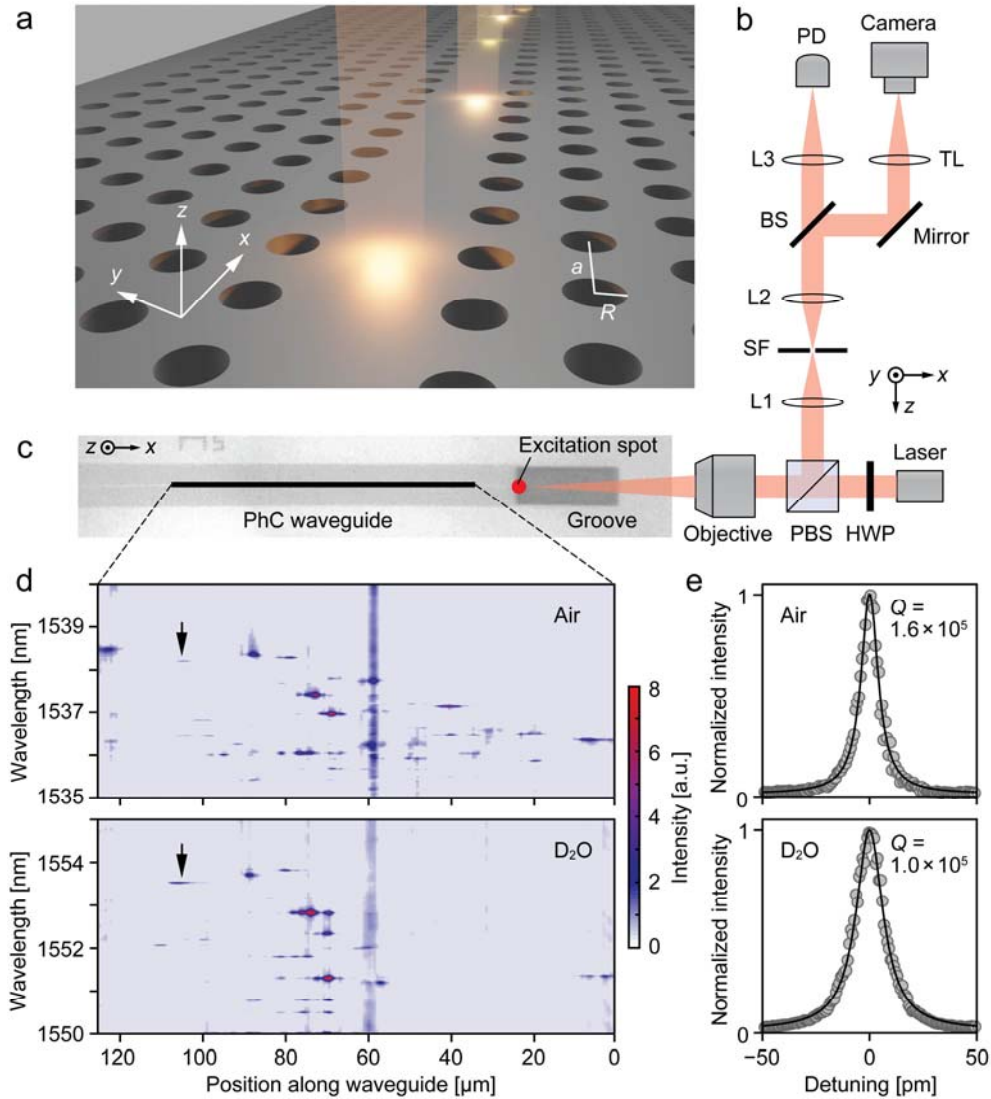
Figure 1. Photonic crystal (PhC) random cavity. a) Schematic illustration of the randomly distributed optical microcavities along the silicon W1 PhC waveguide; *a* and *R* indicate the lattice constant and air-hole radius, respectively. b) Scheme of experimental setup for free-space excitation of Anderson-localized modes and c) a microscopic image of a free-standing W1 PhC waveguide. A tightly focused laser beam with the polarization parallel to the waveguide (red arrow) is focussed from the vertical direction onto the end-facet of the waveguide (red dot) using a 40× objective (NA = 0.6). The vertically scattered light with a polarization that is perpendicular to the waveguide is analyzed using an InGaAs photodiode (PD) and an infrared camera. HWP, half wave plate; PBS, polarizing beam splitter; SP, spatial filter; L, lenses; TL, tube lens. d) Spatially resolved spectra along the PhC waveguide in air (upper, excitation power $P = 1$ mW) and in D_2O (lower, $P = 2$ mW). The approximately 120 μm waveguide section that is imaged on the camera (line scan) is indicated by the black bold line in (c). e) Representative spectra (gray dots) and the Lorentzian fit (black curves) used for the calculation of Q factors of the representative localized modes indicated with the black arrows in (d).

Note that the air-holes of our PhC waveguides have approximately a 4° sidewall tilt revealed by observation with a scanning electron microscope, which explains the quite efficient excitation of localized modes.[41] This vertical asymmetry of the sidewall causes polarization mixing when light propagates along the waveguide.[56,57] As a result, the ballistic TM-like mode can be converted to the TE-like fundamental mode at the intersection of the two modes where the group velocity of TE-like photonic band is small[41,58] and where the Anderson-localized modes appear. In this way naturally created sidewall tilts, and the modest unavoidable fabrication disorder in our sample, favour the efficient excitation of the localized modes.

We validate the Anderson-localization by analyzing the spatial distribution of the intensities of the light scattered by the random microcavities. Here, we consider the variance of the normalized intensity distribution var($I/\langle I \rangle$) where I is the intensity and $\langle I \rangle$ is the ensemble average of the intensity of the light scattered by one waveguide as identified by imaging. Anderson-localization of PhC waveguides can also be characterized by the localization length, which is determined from the exponential decay of the electromagnetic field of the near field,[38] however, the measurement is not always a simple task. For example, it is difficult to discern if the decay originates from the effects of the coherent scattering processes or the material absorption. An alternative Anderson-localization criterion has been introduced which makes it possible to analyse the variance of the intensities in a spectrum and show that var($I/\langle I \rangle$) > 7/3 for Anderson-localization which holds even under the presence of the material absorption.[59] We confirm that this condition is met for our PhC waveguides in a 10 nm spectral window containing the localized modes. We find var($I/\langle I \rangle$) = 14.4 in air and var($I/\langle I \rangle$) = 3.41 in D_2O (see Figure S1 for details).

2.2. Statistical characterization of random microcavities

Q factors of localized modes in air and D_2O were extracted from four different PhC waveguides (N_{sample} = 4) by the Lorentzian fits. **Figure 2**a shows the histograms. The average of the Q factors in D_2O ($\langle Q \rangle$ = 4.1 × 10^4) decreased compared to the measurements in air ($\langle Q \rangle$ = 5.5 × 10^4) due to the reduced refractive index difference between the silicon PhC slab and external medium. At the same time, the total number of localized modes (N_{mode}) in D_2O was smaller than those observed in air, which was consistent with a spatial map of the light scattered from the optical microcavities imaged in Figure 1d. Notably, the maximum Q factor was 3.4 × 10^5 in air and 2.0 × 10^5 in D_2O. These values are in fact close to the ideal Q~10^6 imposed by scattering loss[60] in PhC cavities, indicating that Q factors of Anderson-localized modes in

silicon PhC waveguides are comparable to that would be obtained in carefully engineered and fabricated defect cavities. Next, we measured the wavelength shifts of the localized modes by changing the NaCl concentrations in D_2O, as shown in Figure 2b. As expected, the peak positions of localized modes red-shifted in wavelength with increasing solution refractive index. Although some peaks seem to have split or disappeared, bulk refractive index sensitivities S [nm/RIU] were evaluated, where possible, from the slope of the wavelength shifts $\Delta\lambda$ versus the refractive index changes Δn. From the histogram in Figure 2c, the average of S ($<S>$) was determined to be 79.3 nm/RIU.

S can be estimated from $S = \Gamma_{env}(\lambda_0/n_{eff})$ where Γ_{env} is the confinement factor of the electric field energy stored in the surrounding medium, λ_0 is the cavity resonance wavelength, and n_{eff} is the effective refractive index of the cavity mode.[61,62] Our random cavities have a few times smaller S compared with well-engineered PhC defect cavities which are as high as $S > 500$ nm/RIU,[9,63] which in turn indicates that the Anderson-localized modes are tightly confined inside the silicon slab, i.e., a large Q factor and small Γ_{env}. The slight deviation in S among different random cavities can be accounted for by the fact that each cavity has different Γ_{env} and n_{eff}. Considering a commonly used figure of merit (FOM) expressed as S/FWHM [RIU^{-1}] where FWHM is the full width at half maximum,[64] our random cavities reach up to FOM = 1.0×10^4 RIU^{-1} in D_2O. Refractive index sensing with Anderson-localized modes was first reported in 2017 using a Si_3N_4 PhC waveguide,[47] but the FOM ~270 RIU^{-1} was not as large as is the case here. This can be attributed to the smaller Q factors of Si_3N_4-based cavity modes which is expected because of the refractive index of Si_3N_4 (n ~2) which is much smaller than that of Si (n ~3.5).

At the same Q factor of a microcavity, a smaller mode volume V would give a larger wavelength shift.[65] Although it is difficult to extract individual V of Anderson-localized modes experimentally, theoretical works have shown that the smallest V reaches around $1(\lambda/n)^3$, which corresponds to the diffraction-limited mode volume.[42] Therefore, Q/V is expected to reach up to 2.0×10^5 $(n/\lambda)^{-3}$ in D_2O in our case. As will be shown next, this Q/V is sufficiently large to detect single particles and viruses. Also, this value is competitive with an engineered one-dimensional PhC ($Q/V = 3.0 \times 10^5$ $(n/\lambda)^{-3}$) nanobeam cavity[12] which needed to employ a side coupling using an optical fibre. It should be noted here that further enhancement of Q/V has been experimentally demonstrated with hybrid plasmonic-photonic systems,[13,66] enabling monitoring of single protein interactions.[13]
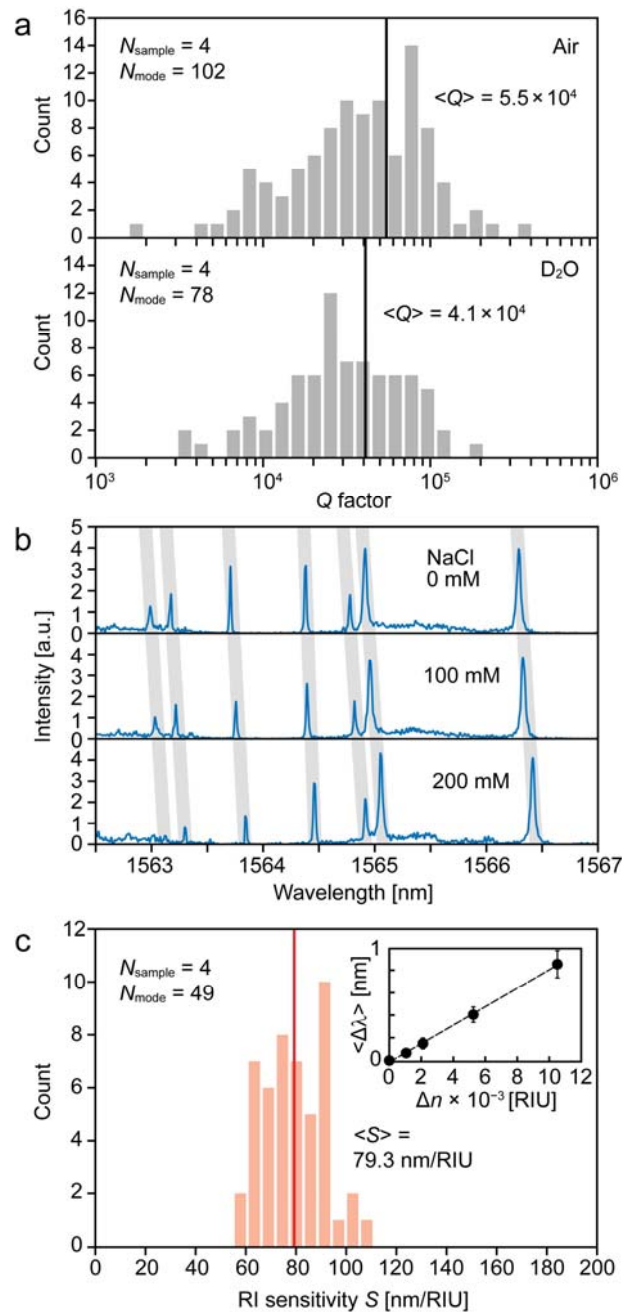
8

Figure 2. Statistical analysis of Q factors and refractive index (RI) sensitivities. a) Histograms of Q factors for the random microcavities measured in air and in D_2O. The Q factors were determined from a total of four different W1 PhC samples ($N_{sample} = 4$) with almost identical structural parameters a and r. The vertical black lines represent the average of Q factors ($<Q>$). b) Examples of spectra measured in different NaCl concentrations. The thick grey lines serve as guide to the eye. c) Histogram of RI sensitivities S. The vertical red line represents the average of S ($<S>$). Inset: The average wavelength shift ($<\Delta\lambda>$) as a function of RI change (Δn) of the solution.

2.3. Detection of single polystyrene particles

To demonstrate detection of single polystyrene (PS) particles, PS nanoparticles with different radii of r = 300 nm, 150 nm, and 50 nm were injected into the sample cell. The silicon PhC surface was not functionalized; the nanoparticle adsorption to the silicon relies entirely on electrostatic interactions of the silicon surface and the PS particles (see Experimental Section). **Figure 3**a shows the wavelength shifts that we tracked for a representative Anderson-localized cavity with a 200 ms time resolution. Discrete wavelength steps were observed for all particle sizes and the step heights increased with increasing particle radius r. As we will validate later, these steps are associated with single PS binding events. In principle there are two factors to consider that can contribute to the observed step heights; one is the distance between the cavity and the adsorbed particle, the other is a one-step, multiple-particle adsorption. In our analysis, we only consider individual PS particles. We did not find that the PS particles form aggregates in the buffer solution (see Experimental Section). Although the injected PS concentration c was kept the same for all samples of different nanoparticle radii r (c = 100 μg/mL) we observed a significant difference in the average rate at which the steps were observed. Specifically, for r = 50 nm PS particles, the step rates were higher 0.054 s^{-1} and a large number of approximately 60 particles were detected from the shift of the cavity in the 20 min measurement time. On the other hand, for r = 150 nm and 300 nm PS particles, the step rates of 0.0044 s^{-1} were low, and the binding events saturated with the adsorption of only approximately 5 particles. We attribute the reduced number of steps to the fact that the larger particle sizes compared with the cavity mode volume, which limits the number of adsorption events in a cavity owing to the limited available binding sites. Another possibility is that the particles are too large to infiltrate the air-holes of the cavity, changing the binding kinetics. Note that the gradual and slight drifts of the resonance wavelengths towards a longer wavelength could be attributed to many factors including slight movement of the optical setup and the evaporation of the sample solution over time.[15]

The average step height for the different size PS particles is shown in the inset of Figure 3b. For r = 50 nm, as there were many steps less than 5 nm, which were imperceptible in Figure 3a, the average step height was much smaller than that for other particle sizes. There was no large difference for the average step heights that were observed for r = 150 nm and 300 nm PS particles. This can be attributed to the fact that the PS particles size is large compared to the evanescent decay length L of the cavity modes (L = 52 nm). For particle radii of tens to hundreds of nm, the wavelength shift of a microcavity $\Delta\lambda$ is estimated from r and L as follows[15,19]: $\Delta\lambda \propto r^3 e^{-r/L}$. By transforming this, one can obtain $\log(<\Delta\lambda>) + r/L = 3\log(r) + constant.$, which has

a linear slope of approximately 3 in the log-log plot. Figure 3c shows a linear fit of the experimental results. When $L = 52$ nm, the correlation coefficient R^2 was 0.97, showing a good agreement between the experiment and theory. This result confirmed that discrete steps were caused by adsorption of single particles. Furthermore, we evaluated the minimum detectable PS particle radius r_{min} to be 34.0 nm from the intersection of the linear fit and the average noise of the wavelength trace <3σ>, where σ is the standard deviation, calculated by 10 points in the trace.

Figure 3c shows the histogram obtained in a ~20 min measurement window for $r = 50$ nm PS particles. Most of the steps were smaller than 15 nm, and the average step height <Δλ> was approximately 7.5 nm. To further investigate the temporal behaviour of the binding events, the cumulative step counts were plotted in Figure 3d. Given that there is only a limited number of binding sites at the start of measurement (N_0), the step rate saturates over time as the available binding sites decreases with time by the adsorption of particles. The fitted curve shows the saturation function $N(t) = N_0(1-\exp(-k_b t))$,[67] which gives us $N_0 = 56$ and $k_b = 0.0028$ s^{-1}, where k_b is the binding rate per reaction site. Although we traced only one cavity mode, the N_0 was unexpectedly large considering the small mode volume of random cavities. This result suggests that PS particles that adsorb outside of the near-field/mode volume of the sensing cavity also affect the wavelength shift. It is also possible that the actual mode volume is larger than expected.[36] A detailed investigation of the physical mechanism is needed and lies outside the scope of this manuscript.
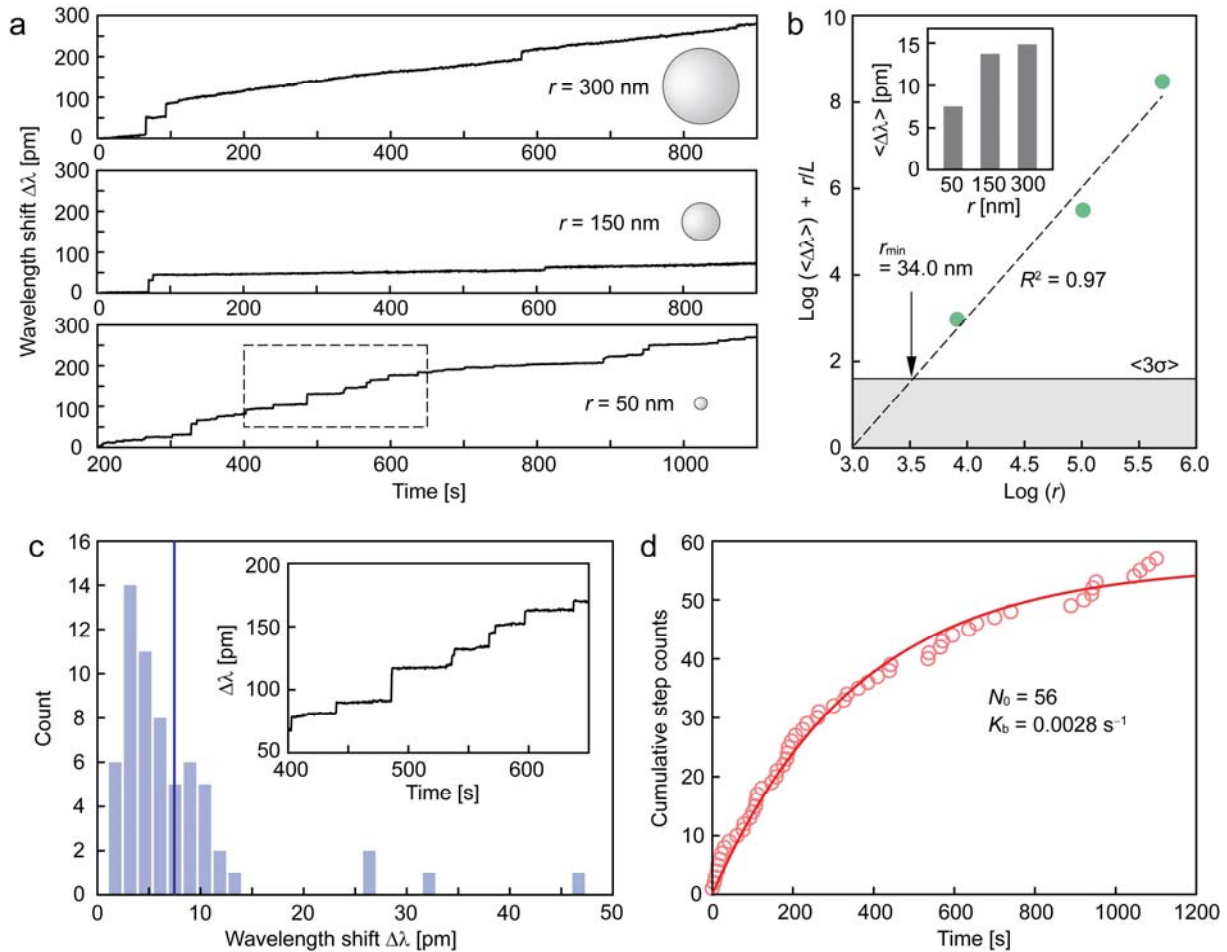
Figure 3. Detection of single polystyrene (PS) particles. a) Resonance wavelength shifts ($\Delta\lambda$) measured by injecting PS particles with radii 300 nm, 150 nm, and 50 nm. Each discrete step is associated with the adsorption of single PS particles onto the PhC waveguide. A single resonance peak of $Q = 4.0 \times 10^4$ in D_2O (100 mM NaCl) was tracked in real-time in these experiments. b) The measured $<\Delta\lambda>$ and the linear fit for different r. The average noise of the wavelength traces $<3\sigma>$ is indicated by the black horizontal line. Minimum detectable PS particle radius $r_{min} = 34.0$ nm was obtained at the intersection of the two lines. Inset: The average of the $\Delta\lambda$ steps ($<\Delta\lambda>$) as a function of r. c) Histogram of wavelength shifts for $r = 50$ nm. The vertical purple line represents the average of $\Delta\lambda$. The inset shows the zoomed-in view of the enclosed region in (a). d) Cumulative step counts for the detection of single PS particles with $r = 50$ nm by tracking the frequency-shift of a single random cavity and the fitted saturation curve.

2.4. Detection of single viruses

The adenovirus solution was injected into a sample chamber and we tracked the wavelength shift of a representative localized mode with $Q = 7.3 \times 10^4$ in D_2O. As shown in **Figure 4**, three different discrete steps were observed in a ~30 min measurement. Note that, similar to the

12

detection of PS particles, the interaction between the silicon surface and the virions relies on the electrostatic interactions between them. To check the reproducibility, we repeated the same measurements three times and obtained the average step height $\langle\Delta\lambda\rangle$ of 3.9 nm. Since adenoviruses have a radius of 35-50 nm[68] and a refractive index smaller than that of PS (~1.59),[69] this step height conforms to the theoretical estimate.

The average noise in the wavelength traces $\langle3\sigma\rangle$ was determined to be 1.0 pm, and thus the signal-to-noise ratio (SNR) for single adenovirus sensing was ~4. Although this value was sufficient to resolve single viruses, the SNR could be improved further by increasing either the Q factor or the peak intensity of the localized mode at the surface of the PhC.[62] In our present study, $\langle3\sigma\rangle$ was about 1/20th the FWHM, but it is predicted to be reduced to 1/2000th the FWHM in an ideal setting for a PhC cavity,[70] which would be 100 times better than is the case here. Improving the sensor response would help more with the reliable detection of single viruses and discriminating their sizes.
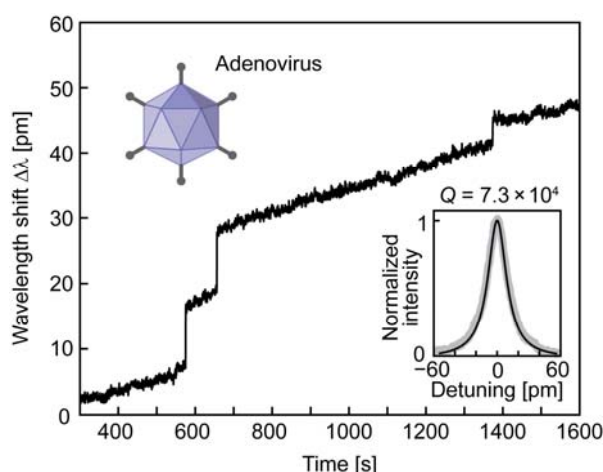

Figure 4. Detection of single adenoviruses. The resonance wavelength shift (pm) vs. time (s). Inset: The measured resonance peak (grey dots) with $Q = 7.3 \times 10^4$ in D_2O (100 mM NaCl) and the corresponding Lorentzian fit (black curve).

3. Conclusion

In this study, we have demonstrated label-free single virus detection on silicon PhC random cavities. The Anderson-localized cavities are excited in W1 PhC waveguides and have resonance Q factors of ~10^5 in D_2O. The single particle detection capability has been confirmed by detecting different sizes of PS particles and single adenoviruses. Given the present experimental parameters, the minimum detectable PS particle radius has been estimated to be around 34 nm. Our high Q/V PhC cavities are excited by a free-space beam and without the

need of elaborate structural optimizations and integration of gratings or delicate fibre couplers, needed in sensing applications with well-engineered PhC defect cavities. One of the limitations of the proposed sensing method is that it is currently not possible to predict the exact number and locations of each of the detectable localized modes. Thus, we have to use imaging to find the random cavities and their location along the guide. Furthermore, because of the large free-spectral range it is difficult to currently track multiple random cavity modes simultaneously. This issue can be addressed by using a larger-bandwidth piezo tuning laser source. The random microcavities can be excited by focussing a fixed single beam onto the W1 waveguide end-facet, which enables multiplexed detection without the need for the spatial scanning of the laser beam.

Taking into account the fact that the presented silicon PhC waveguides are CMOS compatible and made of comparatively inexpensive silicon-on-insulator wafers, this platform may become important for the future on-chip diagnostic devices that require single particle detection capabilities. We envisage that the detection of specific interactions between intact virions and the sensor surface functionalized with a specific antibody or an aptamer[71] will enable a high specificity for multiplexed virus sensing applications. Finally, we should emphasize that isolated PhC chips can be readily integrated with microfluidics that allow detection with small sample volumes and utilising multiple sample channels via automated sample input/output systems.[72] Thus, on-chip virus diagnostic devices with multiplexed detection systems are potentially realizable. The sensitivity range could be extended to the single-molecule level in optoplasmonic Anderson-localized PhC microcavities.[24] While our current work is devoted to the detection of single viruses on a simple sensor chip, the sensing of single proteins sets one of the future directions for this work.

4. Experimental Section

Device Fabrication and characterization: W1 PhC waveguides were fabricated on silicon-on-insulator wafers with a silicon layer of 220 nm thickness. The details of the fabrication process are described elsewhere.[46] Briefly, the triangular lattice PhC patterns, where a line of air-holes was left out to realize W1 waveguide, were defined by electron-beam lithography and then transferred into the wafers using chlorine-based inductively coupled plasma reactive ion etching. The buried oxide layer was finally removed with buffered hydrofluoric acid to form a free-standing PhC slab. Random cavities in the PhC waveguide were excited using a 40× objective (Nikon, NA = 0.6) where the wavelength-scanning of the impinged beam from a tuneable laser was realized by means of built-in motor (Ando, AQ4320D) for broadband

excitation (1480–1580 nm, 100 kHz linewidth and 1 pm tuning resolution). The out-of-plane scattering of the cavity modes was imaged and recorded by an InGaAs camera (Sensors Unlimited, 320CSX). Once a sharp resonance peak to be used for a single particle sensing experiment was determined, the excitation source was switched to a tuneable laser (Spectra Quest Lab, λ-lock) equipped with piezo to precisely scan the wavelengths (1460–1600 nm). A function generator (Hewlett-Packard) was connected to the laser controller to perform the piezo scan with a triangular waveform at 5 Hz for a frequency range of ~100 GHz. The reference signal and the resonance spectra measured with a 1.0 mm diameter InGaAs PD (Edmund Optics, #59-198) at room temperature were acquired by a data acquisition system (National Instruments), and the peak positions were recorded by Lorentzian fitting in real-time.

Detection of single particles: The sample cell was made by tightly sandwiching a silicone rubber sheet between a glass slide and a cover slip after their air plasma treatment. Then, a PhC sample was fixed into the cell by using a silicone glue for measurement in aqueous solution. PS particles solution (Alpha Nanotech, 10 mg/mL, carboxylated) were first centrifuged at 10,000 rpm for 10–15 min and the pellet was re-suspended in D_2O (Merck, 151882). It was then dispersed in an ultrasonic bath for 5 min to separate individual particles. The solution was injected into the sample cell (300 μL) to a final concentration of 100 μg/mL. To minimize the repulsive force between the PS particles and the silicon PhC surface, the solution pH was adjusted to pH ~2 in 100 mM NaCl. Only when comparing the results with different sizes of PS particles (Figure 3), the PS particles were removed from the device by heating it in acetone at 70°C for 20 min, in order to repeat the experiment using the same localized mode. Adenovirus sample was provided by University of Plymouth, and the sample solution was injected into the sample cell filled with D_2O (pH~7, 100 mM NaCl) at a dilution of 1/25.

Preparation of adenovirus solution: Adenovirus vector strain Ad5-GFP, a replication defective Ad5 that does not express adenovirus early region 1A (E1A), was also used as an analyte for single particle sensing. Adenovirus is a common virus that typically causes colds or flu-like symptoms in those infected. Ad5-GFP was obtained via collaboration and grown and purified as described previously.[73] Typical sizes of adenovirus are 100 nm in diameter. The samples were inactivated via germicidal UV-C light at a wavelength of 253.7 nm. The concentration of viral particles stock solution (in PBS) was 1×10^9 pfu/ml.

Supporting Information

Supporting Information is available from the Wiley Online Library or from the author.

References

[1]   B. D. Kevadiya, J. Machhi, J. Herskovitz, M. D. Oleynikov, W. R. Blomberg, N. Bajwa, D. Soni, S. Das, M. Hasan, M. Patel, A. M. Senan, S. Gorantla, J. McMillan, B. Edagwa, R. Eisenberg, C. B. Gurumurthy, S. P. M. Reid, C. Punyadeera, L. Chang, H. E. Gendelman, *Nat. Mater.* **2021**, *20*, 593.

[2]   N. Toropov, E. Osborne, L. T. Joshi, J. Davidson, C. Morgan, J. Page, J. Pepperell, F. Vollmer, *ACS Sensors* **2021**, *6*, 2815.

[3]   L. Huang, L. Ding, J. Zhou, S. Chen, F. Chen, C. Zhao, J. Xu, W. Hu, J. Ji, H. Xu, G. L. Liu, *Biosens. Bioelectron.* **2021**, *171*, 112685.

[4]   G. Qiu, Z. Gai, Y. Tao, J. Schmitt, G. A. Kullak-Ublick, J. Wang, *ACS Nano* **2020**, *14*, 5268.

[5]   B. Zhao, C. Che, W. Wang, N. Li, B. T. Cunningham, *Talanta* **2021**, *225*, 122004.

[6]   T. T. S. Lew, K. M. M. Aung, S. Y. Ow, S. N. Amrun, L. Sutarlie, L. F. P. Ng, X. Su, *ACS Nano* **2021**, *15*, 12286.

[7]   D. Yu, M. Humar, K. Meserve, R. C. Bailey, S. N. Chormaic, F. Vollmer, *Nat. Rev. Methods Prim.* **2021**, *1*, 83.

[8]   M. R. Lee, P. M. Fauchet, *Opt. Express* **2007**, *15*, 4530.

[9]   M. G. Scullion, T. F. Krauss, A. Di Falco, *Sensors* **2013**, *13*, 3675.

[10]   S. Pal, A. R. Yadav, M. A. Lifson, J. E. Baker, P. M. Fauchet, B. L. Miller, *Biosens. Bioelectron.* **2013**, *44*, 229.

[11]   J. E. Baker, R. Sriram, B. L. Miller, *Lab Chip* **2017**, *17*, 1570.

[12]   C. Wang, Q. Quan, S. Kita, Y. Li, M. Lončar, *Appl. Phys. Lett.* **2015**, *106*, 261105.

[13]   F. Liang, Y. Guo, S. Hou, Q. Quan, *Sci. Adv.* **2017**, *3*, 1.

[14]   S. Lin, K. B. Crozier, *ACS Nano* **2013**, *7*, 1725.

[15] Q. Quan, D. L. Floyd, I. B. Burgess, P. B. Deotare, I. W. Frank, S. K. Y. Tang, R. Ilic, M. Loncar, *Opt. Express* **2013**, *21*, 32225.

[16] F. Liang, Q. Quan, *ACS Photonics* **2015**, *2*, 1692.

[17] P. Kang, P. Schein, X. Serey, D. O'Dell, D. Erickson, *Sci. Rep.* **2015**, *5*, 12087.

[18] N. Li, T. D. Canady, Q. Huang, X. Wang, G. A. Fried, B. T. Cunningham, *Nat. Commun.* **2021**, *12*, 1.

[19] F. Vollmer, S. Arnold, D. Keng, *Proc. Natl. Acad. Sci. U. S. A.* **2008**, *105*, 20701.

[20] V. R. Dantham, S. Holler, V. Kolchenko, Z. Wan, S. Arnold, *Appl. Phys. Lett.* **2012**, *101*, 043704.

[21] V. R. Dantham, S. Holler, C. Barbre, D. Keng, V. Kolchenko, S. Arnold, *Nano Lett.* **2013**, *13*, 3347.

[22] F. Vollmer, D. Yu, *Optical Whispering Gallery Modes for Biosensing*, Springer International Publishing, Cham, **2020**.

[23] S. Subramanian, H. B. L. Jones, S. Frustaci, S. Winter, M. W. Van Der Kamp, V. L. Arcus, C. R. Pudney, F. Vollmer, *ACS Appl. Nano Mater.* **2021**, *2021*, 4583.

[24] J. Xavier, S. Vincent, F. Meder, F. Vollmer, *Nanophotonics* **2018**, *7*, 1.

[25] S. J. McNab, N. Moll, Y. A. Vlasov, *Opt. Express* **2003**, *11*, 2927.

[26] M. G. Scullion, M. Fischer, T. F. Krauss, *Photonics* **2014**, *1*, 412.

[27] E. Kim, M. D. Baaske, F. Vollmer, *Lab Chip* **2017**, *17*, 1190.

[28] J. Zhu, Ş. K. Özdemir, L. Yang, *IEEE Photonics Technol. Lett.* **2011**, *23*, 1346.

[29] T. Baba, A. Motegi, T. Iwai, N. Fukaya, Y. Watanabe, A. Sakai, *IEEE J. Quantum Electron.* **2002**, *38*, 743.

[30] J. Topolancik, B. Ilic, F. Vollmer, *Phys. Rev. Lett.* **2007**, *99*, 253901.

[31] Y. N. Zhang, Y. Zhao, R. Q. Lv, *Sensors Actuators, A Phys.* **2015**, *233*, 374.

[32] B.-S. Song, S. Noda, T. Asano, Y. Akahane, *Nat. Mater. 2005 43* **2005**, *4*, 207.

[33] A. Di Falco, L. O'Faolain, T. F. Krauss, *Appl. Phys. Lett.* **2009**, *94*, 063503.

[34] A. Mahdavi, P. Roth, J. Xavier, T. K. Paraïso, P. Banzer, F. Vollmer, *Appl. Phys. Lett.* **2017**, *110*, 241101.

[35] L. Sapienza, H. Thyrrestrup, S. Stobbe, P. D. Garcia, S. Smolka, P. Lodahl, *Science (80-.).* **2010**, *327*, 1352.

[36] H. Thyrrestrup, S. Smolka, L. Sapienza, P. Lodahl, *Phys. Rev. Lett.* **2012**, *108*, 113901.

[37] J. Liu, P. D. Garcia, S. Ek, N. Gregersen, T. Suhr, M. Schubert, J. Mørk, S. Stobbe, P. Lodahl, *Nat. Nanotechnol.* **2014**, *9*, 285.

[38] P. D. García, G. Kiršanskė, A. Javadi, S. Stobbe, P. Lodahl, *Phys. Rev. B* **2017**, *96*,

144201.

[39]   N. Le Thomas, H. Zhang, J. Jágerská, V. Zabelin, R. Houdré, I. Sagnes, A. Talneau, *Phys. Rev. B* **2009**, *80*, 125332.

[40]   S. Mazoyer, J. P. Hugonin, P. Lalanne, *Phys. Rev. Lett.* **2009**, *103*, 063903.

[41]   J. Topolancik, F. Vollmer, R. Ilic, M. Crescimanno, *Opt. Express* **2009**, *17*, 12470.

[42]   J. P. Vasco, S. Hughes, *Phys. Rev. B* **2017**, *95*, 224202.

[43]   J. Liu, P. D. Garcia, S. Ek, N. Gregersen, T. Suhr, M. Schubert, J. Mørk, S. Stobbe, P. Lodahl, *Nat. Nanotechnol.* **2014**, *9*, 285.

[44]   H. Thyrrestrup, S. Smolka, L. Sapienza, P. Lodahl, *Phys. Rev. Lett.* **2012**, *108*, 113901.

[45]   J. Gao, S. Combrie, B. Liang, P. Schmitteckert, G. Lehoucq, S. Xavier, X. Xu, K. Busch, D. L. Huffaker, A. De Rossi, C. W. Wong, *Sci. Rep.* **2013**, *3*, 1.

[46]   F. Vollmer, J. Topolancik, *Laser Reson. Beam Control X* **2008**, *6872*, 68720X.

[47]   O. J. Trojak, T. Crane, L. Sapienza, *Appl. Phys. Lett.* **2017**, *111*, 141103.

[48]   M. Notomi, K. Yamada, A. Shinya, J. Takahashi, C. Takahashi, I. Yokohama, *Phys. Rev. Lett.* **2001**, *87*, 253902.

[49]   H. S. Dutta, A. K. Goyal, V. Srivastava, S. Pal, *Photonics Nanostructures - Fundam. Appl.* **2016**, *20*, 41.

[50]   E. Kuramochi, M. Notomi, S. Hughes, A. Shinya, T. Watanabe, L. Ramunno, *Phys. Rev. B - Condens. Matter Mater. Phys.* **2005**, *72*, 161318.

[51]   L. O'Faolain, T. P. White, D. O'Brien, X. Yuan, M. D. Settle, T. F. Krauss, *Opt. Express* **2007**, *15*, 13129.

[52]   K. Rivoire, A. Faraon, J. Vuckovic, *Appl. Phys. Lett.* **2008**, *93*, 063103.

[53]   D. Englund, A. Majumdar, A. Faraon, M. Toishi, N. Stoltz, P. Petroff, J. Vučković, *Phys. Rev. Lett.* **2010**, *104*, 073904.

[54]   M. Galli, S. L. Portalupi, M. Belotti, L. C. Andreani, L. O'Faolain, T. F. Krauss, *Appl. Phys. Lett.* **2009**, *94*, 071101.

[55]   L. Huang, H. Tian, D. Yang, J. Zhou, Q. Liu, P. Zhang, Y. Ji, *Opt. Commun.* **2014**, *332*, 42.

[56]   Y. Tanaka, T. Asano, Y. Akahane, B. S. Song, S. Noda, *Appl. Phys. Lett.* **2003**, *82*, 1661.

[57]   J. Canning, N. Skivesen, M. Kristensen, L. H. Frandsen, A. Lavrinenko, C. Martelli, A. Tetu, *Opt. Express* **2007**, *15*, 15603.

[58]   S. R. Huisman, G. Ctistis, S. Stobbe, A. P. Mosk, J. L. Herek, A. Lagendijk, P. Lodahl, W. L. Vos, P. W. H. Pinkse, *Phys. Rev. B* **2012**, *86*, 155154.

[59] A. A. Chabanov, M. Stoytchev, A. Z. Genack, *Nature* **2000**, *404*, 850.

[60] A. Simbula, M. Schatzl, L. Zagaglia, F. Alpeggiani, L. C. Andreani, F. Schäffler, T. Fromherz, M. Galli, D. Gerace, *APL Photonics* **2017**, *2*, 056102.

[61] H. Zhu, I. M. White, J. D. Suter, P. S. Dale, X. Fan, *Opt. Express* **2007**, *15*, 9139.

[62] I. M. White, X. Fan, *Opt. Express* **2008**, *16*, 1020.

[63] G. Pitruzzello, T. F. Krauss, *J. Opt.* **2018**, *20*, 073004.

[64] J. N. Anker, W. P. Hall, O. Lyandres, N. C. Shah, J. Zhao, R. P. Van Duyne, *Nat. Mater.* **2008**, *7*, 442.

[65] S. Arnold, M. Khoshsima, I. Teraoka, S. Holler, F. Vollmer, *Opt. Lett.* **2003**, *28*, 272.

[66] D. Conteduca, C. Reardon, M. G. Scullion, F. Dell'Olio, M. N. Armenise, T. F. Krauss, C. Ciminelli, *APL Photonics* **2017**, *2*, 086101.

[67] E. Kim, M. D. Baaske, F. Vollmer, *Adv. Mater.* **2016**, *28*, 9941.

[68] B. Saha, C. M. Wong, R. J. Parks, *Viruses* **2014**, *6*, 3563.

[69] Y. Pang, H. Song, W. Cheng, *Biomed. Opt. Express* **2016**, *7*, 1672.

[70] K. Saurav, N. Le Thomas, *Optica* **2017**, *4*, 757.

[71] V. T. Nguyen, H. Bin Seo, B. C. Kim, S. K. Kim, C. S. Song, M. B. Gu, *Biosens. Bioelectron.* **2016**, *86*, 293.

[72] Z. Liao, Y. Zhang, Y. Li, Y. Miao, S. Gao, F. Lin, Y. Deng, L. Geng, *Biosens. Bioelectron.* **2019**, *126*, 697.

[73] G. Fejér, K. Szalay, I. Győry, M. Fejes, E. Kúsz, S. Nedieanu, T. Páli, T. Schmidt, B. Siklódi, G. Lázár, G. Lázár, E. Duda, *J. Immunol.* **2005**, *175*, 1498.